Distinction between small RNA-bound and free ARGONAUTE via an N-terminal protein-protein interaction site

Simon Bressendorff[1,4], Ida Marie Zobbe Sjøgaard[1,4], Emilie Duus Oksbjerg[1], Swathi Kausika[1], Alec Michels[1], Andreas Prestel[2], Birthe B. Kragelund[2], Christian Poulsen[1,3] and Peter Brodersen[1,5]

[1]Copenhagen Plant Science Center, University of Copenhagen

[2]Structural Biology and NMR Laboratory, Department of Biology, University of Copenhagen

[3]Present address: Novo Nordisk A/S,

[4]These authors contributed equally to this work

[5]Corresponding author, email pbrodersen@bio.ku.dk

Abstract

ARGONAUTE (AGO) proteins bind to small non-coding RNAs to form RNA Induced Silencing Complexes (RISCs). In the RNA-bound state, AGO proteins are stable while RNA-free AGOs undergo regulated proteolysis or associate with chaperones *en route* to RISC maturation. Molecular determinants unique to RNA-free AGO that allow its specific recognition and degradation remain poorly characterized. Here, we show that the Arabidopsis autophagy cargo receptor ATI1 interacts with unloaded AGO1 via multiple interaction sites that include direct contact to a confined, linear region in AGO1, the N-coil. The N-coil is accessible to antibodies preferentially in the RNA-free state of AGO1, and influences its degradation rate *in vivo*. These results provide insight into the molecular basis for specific recognition of the RNA-free state of eukaryotic AGO proteins, and introduce a new tool for its further study.

Introduction

RNA Induced Silencing Complexes (RISCs) are central components in the processing of genetic information in eukaryotes. The minimal RISC consists of an ARGONAUTE (AGO) protein bound to a small non-coding RNA that guides RISC to complementary target RNAs by base pairing. In turn, RISCs repress gene expression sequence-specifically using a variety of mechanisms operating at either transcriptional or post-transcriptional levels. The exact properties of RISCs in these contexts are determined by several factors including the identity of the AGO protein, RISC co-factors, and the degree of small RNA:target RNA base pairing[1]. In animals, two distinct phylogenetic clades of AGO proteins exist. The Piwi clade is primarily used for silencing of transposable elements in the germline via Piwi-interacting RNAs (piRNAs)[2]. The Ago clade carries out endogenous gene regulation, in the main via microRNAs (miRNAs)[3], and, in particular in invertebrates, basic antiviral defense via virus-derived small interfering RNAs (siRNAs)[4]. Plants encode only Ago-clade proteins, and use several distinct, functionally specialized AGO proteins. For example, the AGO4/6/9 clade binds to siRNAs from transposable elements to form RISCs that affect transcriptional silencing by directing DNA methylation[5]. miRNAs mediate post-transcriptional regulation via cleavage or translational repression of mRNAs mainly in association with AGO1 with additional specialized, yet important, roles of AGO2, AGO7 and AGO10 (reviewed in [6]). Finally, antiviral RNA interference is carried out by AGO1, AGO2 and AGO5, and, potentially, by several additional AGO proteins[7-11].

All AGO proteins consist of four separate domains called N, PAZ, MID and Piwi[1]. They fold into a two-lobed structure in the small RNA-bound state with N and PAZ together in one lobe and MID/Piwi in the other[12-15] (Fig. 1). The ends of the small RNA are tethered in dedicated binding pockets in the MID and PAZ domains such that the 5'-end is bound to MID[16,17] and the 3'-end to PAZ[18]. PAZ and MID are connected by a long linker sequence called L2 that also interacts extensively with the small RNA backbone and with other AGO domains in the small RNA-bound state[13-15] (Fig. 1).

The assembly of RISC by incorporation of a small RNA into AGO, referred to as "RISC loading", is a critical event in all RNA silencing pathways. This process requires the Hsp40-Hsp70-Hsp90 chaperone assembly line in such a way that association of unloaded AGO with chaperones extends the dwell time of encounters between AGO and small RNA duplexes[19-23]. The chaperone assistance vastly increases the probability of a small RNA

duplex:AGO encounter to lead to formation of a long-lived AGO:small RNA duplex intermediate that subsequently matures into RISC with a single-stranded RNA by duplex unwinding[23], sometimes requiring passenger strand cleavage catalyzed by AGO[24-27]. The loading process constitutes a key regulatory point in RNA silencing. First, it is rate-limiting for biogenesis of many miRNAs *in vivo*[28]. Second, in many organisms including mammals, *C. elegans, Drosophila* and *Arabidopsis*, it is decisive for the stability of AGO proteins. Small RNA-bound AGO (RISC) is stable, but unloaded AGO is rapidly degraded *in vivo*[29-31], unless it exists as an Hsp90 complex *en route* to loading[31,32]. Although it is clear that both the ubiquitin-proteasome pathway and selective autophagy are involved in turnover of unloaded AGO both in plants and animals[29-34], two key questions remain poorly elucidated: (1) What are the molecular determinants that distinguish loaded from unloaded AGO to allow selective degradation of unloaded AGO? (2) What is the biological importance of eliminating unloaded AGO?

The first question has been approached in studies of the *Drosophila* miRNA effector Ago1, whose unloaded form is ubiquitinated in the L2 region by the RING finger protein Iruka[35]. This finding highlights L2 as a region of importance for distinction between loaded and unloaded AGO. It is, however, unlikely to be easily generalized to other systems, because the site of ubiquitination is non-conserved, and, in particular, is adjacent to a *Dm*Ago1-specific deletion in L2 compared to other miRNA-interacting AGO proteins (Supplemental Fig. 1). The second question remains unresolved, but it is widely assumed that avoidance of loading of RNA degradation fragments into AGO that may initiate unwanted RISC-mediated repression or compete with *bona fide* miRNAs for AGO binding is a major driver of mechanisms targeting unloaded AGO for proteolysis[29,30,35]. This hypothesis is indirectly supported by several lines of evidence, although clear observations of ectopic or reduced RISC function upon inactivation of factors involved in AGO degradation have not been reported. For example, mutation of the *Arabidopsis* F-box protein FBW2 restores steady-state levels of an AGO1 mutant protein predicted to have a destabilized fold of the PAZ domain[36]. It is, however, unclear whether FBW2 targets AGO1 directly, and whether it specifically mediates degradation of unloaded, but functional AGO1, or plays a more general role in chaperone-assisted protein degradation elicited as a consequence of partial unfolding of the PAZ domain in the point mutant analyzed. In addition, mutations in key components of miRNA biogenesis had to be introduced to observe relatively minor

95 changes in populations of AGO1-loaded small RNAs upon inactivation of *FBW2*, and no
96 causal relationships between illegitimate siRNAs bound to AGO1 and phenotypes could be
97 established[36]. Similarly, the efficiency of miRNA-guided target mRNA repression was only
98 modestly reduced in *Drosophila* S2 cells upon depletion of Iruka[35].
99 In this study, we use the *Arabidopsis* miRNA effector AGO1 to define a region of
100 crucial importance in the distinction between eukaryotic AGO proteins in the RNA-bound
101 and in the free state. We show that the N-coil, a small, highly conserved linear region
102 towards the N-terminus of AGO1, yet part of the MID-Piwi lobe in the loaded conformation,
103 is preferentially accessible in unloaded AGO1. Furthermore, the N-coil functions as a direct
104 binding site for the autophagy cargo receptor ATG8 INTERACTING PROTEIN1 (ATI1). This
105 highlights the N-coil as a key determinant of the distinction between loaded and unloaded
106 AGO1, and, given its conservation and structural properties, probably in other eukaryotic
107 AGO proteins in both Ago and Piwi clades.
108
109 **Results**
110 *Definition and properties of structural units of the N-terminal part of AGO1*
111 *Arabidopsis thaliana* (At) AGO1 has a 176-aa extension at its N-terminus, in addition to the
112 canonical N-PAZ-MID-PIWI domains found in all AGO proteins. Because this extension is
113 predicted to be an intrinsically disordered region (IDR, Supplemental Fig. 2), we term this
114 part of AGO1 the N-IDR. The N-IDR is followed by a 14-aa region (F177-K190) that we
115 previously termed the N-coil[6]. The N-coil is of interest for a number of reasons: (i) Despite
116 its location in the N-terminal part of AGO in sequence, it is part of the MID-PIWI lobe in
117 structures of AGO-small RNA complexes (Fig. 1a,b). (ii) The N-coil assumes an extended
118 conformation with no secondary structure, yet has low structural flexibility, and reaches
119 across the width of the entire AGO-small RNA complex (Fig. 1b). (iii) Residues in the
120 conserved N-coil are structurally fixed by numerous inter-domain interactions in the AGO-
121 small RNA complex, and the N-coil interface is only moderately hydrophobic with several
122 residues calculated to prefer a hydrophilic environment (Fig. 1c). For example, R182
123 participates in a salt bridge deep inside of the PIWI domain (Fig. 1d), perhaps suggesting
124 that the conformation of the N-coil revealed in the crystal structures of AGO-small RNA
125 complexes is but one of several possible conformations of this region. (iv) The N-coil is
126 functionally important because two mutations in this region have been recovered in forward

127 screens in plants: *ago1-38* (G186R) that exhibits relatively weak loss of function, and shows
128 lower abundance in membrane compartments compared to wild type[37,38], and *ago1-55*
129 (G189E) that exhibits stronger loss of AGO1 function[39]. The N-coil is followed by two β-
130 strands and the globular N-domain (Fig. 1b). The key functional importance of the N-coil and
131 the connecting β-strands is underscored by the observation that substitution of this part of
132 the catalytically inactive human Ago1 by the corresponding part of the catalytically active
133 Ago2 is sufficient to confer activity on an Ago1 variant containing all four residues required
134 for coordination of the two catalytic metal ions[40]. Despite these indications of functional
135 importance of the N-coil region, the precise functions of the entire N-coil-Globular N (NcGN)
136 part of AGO proteins remain ill-defined. Functions of the globular N-domain itself are
137 particularly poorly understood, although the absence of mutations recovered in this part in
138 forward genetic screens reporting on siRNA/miRNA function in plants hints that its functions
139 are not central to the core biochemical properties such as small RNA binding and target
140 RNA cleavage[6].
141
142 *The N-coil-Globular N part of AGO1 interacts with multiple factors implicated in regulated*
143 *proteolysis and functions as a degron*
144 To reveal functions of the poorly understood NcGN part of Arabidopsis AGO1, we first
145 conducted yeast two-hybrid screens with NcGN as a bait against three prey cDNA libraries.
146 This effort yielded 15 potential AGO1-NcGN interactors, all validated in the two-hybrid
147 system by isolation of the prey plasmid and re-transformation with AGO1 NcGN bait into the
148 reporter strain (Supplemental Fig. 3, Table S1). Several candidate interactors had predicted
149 biochemical functions related to regulated proteolysis via either the ubiquitin-proteasome
150 pathway or via autophagy (Table S1). This also included the two intrinsically disordered,
151 transmembrane autophagy cargo receptor proteins ATI1 and ATI2[41,42] that were previously
152 shown to be implicated in degradation of AGO1 via the poleroviral RNAi suppressor P0[43].
153 The trend towards protein degradation was not exclusive, however, as other interactors were
154 also recovered, including Hsp90, a protein phosphatase, and vesicle trafficking and
155 membrane contact proteins (VAP27, NTMC2T5.1)[44,45] (Table S1). Nonetheless, since
156 "Regulated proteolysis" was the clearest common functional category among candidate
157 interactors, we carried out pulse labeling experiments with yellow fluorescent protein (YFP)
158 and NcGN-YFP fusions stably expressed in *Arabidopsis thaliana* to see whether the NcGN

159 in isolation could cause rapid degradation. When lines with similar YFP steady state levels
160 were compared, the synthesis rate (and hence also the degradation rate) of the NcGN-YFP
161 fusion protein was indeed 6.6-fold higher than YFP alone, demonstrating that the NcGN is
162 subject to rapid proteolysis (Supplemental Fig. 4). We note that recognition of NcGN by the
163 chaperone-assisted protein degradation machinery as a consequence of its detachment
164 from normally interacting domains in native AGO1 is unlikely, because the $Gal4^{BD}$-NcGN
165 fusion protein was easily detectable in yeast (Supplemental Fig. 4), and was sufficiently
166 stable for yeast two-hybrid analyses to be carried out. Thus, we focused our attention on the
167 role of the NcGN in regulated proteolysis of the AGO1 protein.
168
169 *Most candidate NcGN interactors are specific for AGO1*
170 The AGO protein family contains 10 paralogs in Arabidopsis, of which AGO4 is distantly
171 related while AGO10 is very closely related to AGO1. We therefore first used the NcGNs of
172 AGO4 and AGO10 to test whether a subset of the identified candidate interactors (ATI1,
173 ATI2, AUF1, AUF3, UBI, HUB1, PP2C and Hsp90-3, see Table S1) were specific to the
174 NcGN of AGO1 or whether they represented generic AGO NcGN binding proteins. Seven
175 of the candidates (ATI1, ATI2, AUF1, AUF3, UBI, HUB1, PP2C) showed yeast two-hybrid
176 interactions preferentially or exclusively with the NcGN of AGO1, while one (Hsp90-3)
177 interacted with the NcGN of all three proteins (Fig. 2a, Supplemental Fig. 5). These results
178 indicate that most of the candidate interactors isolated by yeast two-hybrid screening are
179 specific to AGO1. We also note that the more general AGO NcGN interaction observed with
180 Hsp90-3 is consistent with the involvement of Hsp90 in the loading of different AGO proteins
181 across organisms[19-21].
182
183 *The N-coil is of special importance for interactions via the NcGN*
184 Since two mutations with functional impact have been identified in the N-coil of AGO1
185 (G186R, G189E) [37,39], we tested whether the 14-aa N-coil may play a role in binding to some
186 of the interactors. We initially screened the interactors for ability to interact with the NcGN
187 carrying the G186R mutation. Surprisingly, this point mutation in the N-coil resulted in
188 strongly reduced interaction with most candidates as measured by β-galactosidase activity
189 originating from *lacZ* expressed under UAS_{Gal} control in the reporter strain (Fig. 2b). Indeed,
190 of five proteins tested (ATI1, ATI2, TCTP, AUF1 and Hsp90) only Hsp90 and AUF1 showed

191 clear interaction upon deletion of the N-coil (Supplemental Fig. 6). On the other hand, with
192 the exception of Hsp90, the N-coil was not sufficient for interaction with any candidate
193 (Supplemental Fig. 6). Because these results point to a special importance of the 14-aa N-
194 coil in several protein-protein interactions, we focus the remainder of the study on defining
195 the properties of the N-coil that underlie its importance in protein-protein interactions
196 involving AGO1. To this end, we chose the NcGN-mediated interaction with the
197 transmembrane ATI1 and ATI2 proteins as our model system, and focused on the IDRs of
198 those proteins, because they define their cytoplasmic part[42]. Furthermore, conditions for
199 their heterologous expression and purification have been established [42].
200
201 *Mapping of residues important for ATI1/ATI2 interaction across the entire NcGN*
202 To identify amino acid residues in the AGO1 NcGN required for ATI1/2 interaction, we first
203 inspected alignments between AGO1 orthologues from many different plant species and
204 between *Arabidopsis* AGO1 and its closest paralogue, AGO10 (Fig. 3a). This analysis
205 revealed multiple sites of variation between AGO1 and AGO10 concentrated in the N-coil
206 and in distinct sites in the GN-domain (Fig. 3a). Several of these sites corresponded to
207 surface-exposed patches, consistent with an involvement in protein-protein interaction (Fig.
208 3b). We therefore constructed a series of point mutants in AGO1 NcGN residues variable
209 between AGO1 and AGO10, and tested the interaction in the yeast two-hybrid system with
210 ATI1 and ATI2. The results showed that multiple residues in the N-coil (K178, K185, K190)
211 and in a few surface-exposed patches of the globular N-domain (P259, M304/E307,
212 especially E307) are required for interaction with ATI1/2 (Fig. 3c, Supplemental Fig. 7-8). In
213 particular, mutation of either lysine residue to glutamic acid throughout the N-coil (K178E,
214 K185E, K190E) disrupted the NcGN-ATI interaction. We therefore moved on to assess the
215 effect of these residues more quantitatively, and to test whether they interacted directly with
216 the IDR of ATI1.
217
218 *The K178E N-coil mutation decreases the NcGN:ATI1-IDR affinity by about 4-fold*
219 We first expressed and purified the IDR of ATI1[42] and wild type and K178E mutant versions
220 of the NcGN of AGO1 fused to SUMO (Fig. 4a), and used these purified proteins for
221 quantitative binding assays by microscale thermophoresis. This assay uses the distinct
222 thermophoretic mobility of different molecular entities to measure the percentage of complex

223 formed between a fluorescently labeled component, and a partner protein added in
224 increasing concentrations from none (0% complex) to an estimated 100-fold molar excess
225 (~100% complex). In our experimental set-up, His_6-SUMO-AGO1 NcGN (WT or K178E) was
226 fluorescently labeled on the unique Cys192 residue close to the N-coil, and the unlabeled
227 IDR of ATI1 was added in increasing quantities. Using this set-up, we confirmed that the
228 interaction between AGO1 NcGN and ATI1-IDR is direct, and measured the dissociation
229 constant to be 11±2 μM (Fig. 4b). Remarkably, these affinity measurements did not
230 necessitate application of a thermal field to measure differential molecular movement,
231 because the fluorescence intensity itself was sensitive to addition of ATI1 (Fig. 4c). This
232 observation suggests that in the AGO1 NcGN-ATI1-IDR complex, the C192-linked
233 fluorophore is located in a distinct chemical environment compared to the free AGO1 NcGN,
234 and thus, close to an interaction site. Indeed, when the N-coil mutant K178E was analysed
235 in the same assay, both the affinity of the ATI1-IDR interaction (47±12 μM), and, especially,
236 the change of fluorescence upon complex formation were substantially reduced (Fig. 4b,c).
237 Taken together with the results of the mutational analyses conducted using yeast two-hybrid
238 assays, these observations indicate that the N-coil is a direct site of interaction between
239 AGO1-NcGN and ATI1-IDR, and that it contributes substantially to the affinity of the
240 interaction.
241
242 *Residues in the N-coil interact directly with the IDR of ATI1*
243 To show conclusively that the N-coil is a direct interaction site of ATI1-IDR, we expressed
244 and purified an ^{15}N-labeled N-coil peptide (172-SSSKAFKFPMRPGKGQSGKRC-192) to
245 perform 2D ^{1}H-^{15}N heteronuclear single quantum coherence nuclear magnetic resonance
246 (NMR) spectroscopy in the presence and absence of the ATI1-IDR. These experiments
247 showed that the signal intensities from backbone amide N-H nuclei of several residues in
248 the N-coil, in particular the N-terminal part from F177-K185, and to a lesser extent the C-
249 terminal K190, were strongly reduced upon addition of ATI1-IDR (Fig. 4d,f), indicating that
250 these residues participate directly in the interaction. Consistent with the importance of K178
251 for the ATI1-IDR interaction, such loss of signal was markedly less pronounced upon
252 addition of ATI1-IDR to an ^{15}N-labeled N-coil peptide containing the K178E mutation, in
253 particular for the amide group of residue 178 (K/E) itself (Fig. 4d-h). We conclude that the
254 N-coil is a direct interaction site of the ATI1-IDR, and that the interaction involves contacts

255 along the entire N-coil, including the K178, K185, and K190 residues. This is noteworthy,
256 because these residues are not spatially close in the high-confidence Alphafold structure of
257 AGO1 in the small RNA-bound conformation (Fig. 3b). Rather, the positions of these
258 residues span the entire width of AGO1, and, given the close N-coil-Piwi domain contacts,
259 define a large surface area of AGO1 in this conformation (Fig. 1a,b). Taken together with
260 the observation that each of these lysines contributes measurably to the interaction (Fig. 3-
261 4, Supplemental Fig. 7), it is a plausible hypothesis that in the ATI1-interacting conformation
262 of AGO1, the N-coil is detached from the remainder of the AGO1 protein, i.e. different from
263 the small RNA-bound conformations captured by X-ray crystallography. We therefore
264 moved on to study the AGO1-ATI1-IDR interaction in the context of full length AGO1, and
265 set out to include analyses of both small RNA-bound and free AGO1.
266
267 *ATI1 interacts with unloaded AGO1 in vivo and the binding implicates N-coil residues*
268 To generate small RNA-free AGO1, we engineered the Y691E mutant, mutated in a key
269 residue in the MID domain that stacks with the 5'-uridine ring of the small RNA, and
270 coordinates the 5'-phosphate of the small RNA. In other Ago proteins, the equivalent
271 mutation leads to complete loss of small RNA binding[34,46]. We used stable transgenic lines
272 in *Arabidopsis* to establish that the Y691E mutant indeed is unloaded. When expressed in
273 the *ago1-3* knockout background, the mutant protein failed to rescue the knockout mutant
274 phenotype, demonstrating total loss of function (Supplemental Fig. 9). In addition,
275 immunoprecipitation of wild type and Y691E mutant protein followed by polynucleotide
276 kinase-mediated labeling of co-purified small RNA showed that in contrast to $AGO1^{WT}$, no
277 small RNA was bound by the $AGO1^{Y691E}$ protein (Supplemental Fig. 9).
278 Because heterologous expression of AGO1 failed, even with the use of a variety of
279 expression hosts (*E. coli*, baculovirus/*Sf-9*, *Schizosaccharomyces pombe*) and
280 affinity/solubilization tags, we used bimolecular fluorescence complementation (BiFC)
281 assays upon transient expression in *Nicotiana benthamiana* for assessment of ATI1
282 interaction with $AGO1^{WT}$ and $AGO1^{Y691E}$. The close AGO1 paralogue, AGO10, was used as
283 a negative control. With $AGO1^{WT}$ fused to the C-terminal part of YFP and ATI1 fused to its
284 N-terminal part (C-YFP-$AGO1^{WT}$ and N-YFP-ATI1), weak, but specific signal was detected
285 in association with the endoplasmic reticulum (ER; Fig. 5a), consistent with previous reports
286 of ATI1-localization to ER-associated ATI-bodies, and with peripheral ER-association of

287 AGO1 [47,48]. We detected a consistent and statistically significant reduction in intensity of the
288 BiFC signal when the C-YFP-AGO1$^{K185E/K190E}$ mutant containing substitutions in N-coil
289 residues implicated in ATI1 binding was used (Fig. 5a,b; Supplemental Fig. 10). We next
290 compared patterns of BiFC signal obtained with C-YFP-AGO1^{Y691E}/N-YFP-ATI1 and C-YFP-
291 AGO1$^{Y691E/K185E/K190E}$/N-YFP-ATI1. With both forms, specific signal was detected, and,
292 similar to what we observed with the wild type AGO1 capable of small RNA binding, the
293 K185E/K190E N-coil mutations resulted in significantly reduced BiFC signal intensity (Fig.
294 5a,b). These results demonstrate that ATI1 interacts with the unloaded form of AGO1, and
295 that N-coil residues contribute to this interaction *in vivo*. We note that complete disruption of
296 ATI1-AGO1 interaction is not expected upon mutation of N-coil residues, because a previous
297 study showed yeast two-hybrid interactions between ATI1 and AGO1 involving both N-PAZ
298 and MID-Piwi lobes of the protein[43]. We also note that the results show that ATI1 is capable
299 of interacting with unloaded AGO1, and may possibly only interact with the unloaded form,
300 because wild type AGO1 exists as a mixed population *in vivo*, mostly of the RNA-bound
301 form, but also with a minor fraction in the unloaded form (see below). Clearly, however, such
302 possible exclusive interaction with unloaded AGO1 is not established by the BiFC assays.
303
304 *Defective ATI1 interaction sites in the NcGN reduce the degradation rate of unloaded AGO1*
305 We next asked whether the interaction sites in the AGO1 NcGN defined by our analyses
306 thus far had an effect on the turnover of unloaded AGO1 *in vivo*. We first generated stable
307 transgenic plants constitutively expressing NcGN-YFP fusions with or without mutations
308 found to disrupt ATI1/ATI2 binding. The AGO1-NcGN wild type construct was also
309 expressed in *ati1/ati2* double knockout backgrounds (Supplemental Fig. 11) to test the
310 possible implication of these two specific NcGN interactors in the turnover of AGO1.
311 Comparisons of NcGN^{WT}-YFP, NcGN$^{K178E/K185E/K190E}$-YFP and
312 NcGN$^{K178E/K185E/K190E/P259E/M304E/E307A}$ protein and mRNA levels showed that the NcGN
313 mutants indeed had higher protein/mRNA ratios than their wild type counterpart (Fig. 6a,
314 Supplemental Fig. 11). This effect could not be explained by different YFP siRNA levels
315 (Supplemental Fig. 11), and is therefore consistent with slower protein degradation *in vivo*.
316 Higher protein/mRNA ratios were also found for AGO1 NcGN in the *ati1*/*ati2* knockout
317 background compared to wild type, although the effect was less pronounced than with NcGN
318 mutants, as expected. Thus, we moved on to test the relevance of the NcGN for degradation

319 of the full-length, unloaded AGO1 protein using pulse-labeling analysis to extract kinetic
320 information directly. To maximize chances of measuring an effect *in vivo*, we used the
321 K185E/K190E/M304E/E307A (henceforth, KKME) mutant with residues important for ATI1/2
322 interaction substituted both in the N-coil and in the globular N-domain. Thus, stable
323 transgenic lines expressing equal steady-state levels of FLAG-AGO1^{WT}, FLAG-AGO1^{Y691E},
324 and FLAG-AGO1$^{Y691E/KKME}$ were selected as material for kinetic analyses (Supplemental Fig.
325 12). We first considered the possible kinetic pathways of newly synthesized AGO1^{WT} and
326 AGO1^{Y691E}. Because AGO1^{WT} can be degraded either prior to or after small RNA loading,
327 (Fig. 6b), the labeling data must be fitted to a sum of two exponentials, with half-lives
328 corresponding to unloaded (minor fraction, 8.5±1.8%, see Methods) and loaded states
329 (major fraction, 91.5±1.8%, see Methods), respectively. In contrast, labeling of the unloaded
330 AGO1^{Y691E} is expected to follow mono-exponential kinetics. Initial analyses indicated that
331 ^{35}S-Met/Cys labeling of entire seedlings resulted in uniform distribution of label within 15
332 minutes (Supplemental Fig. 13), but that a classical pulse-chase set-up was not feasible,
333 because incorporation continued after addition of the chase. Since synthesis and
334 degradation rates are equal at steady state, we decided to do pulse-labeling experiments
335 and measure protein half-lives from incorporation rates of ^{35}S-label/total AGO1 protein in
336 FLAG immunoprecipitations following addition of ^{35}S-Met/Cys label (see Methods). We first
337 compared FLAG-AGO1^{WT} and FLAG-AGO1^{Y691E} lines expressing comparable levels of
338 FLAG-AGO1 at steady state (Fig. 6c,d). This analysis showed that wild type AGO1 indeed
339 exhibits two-phase kinetic behavior. Gratifyingly, the half-life of the rapid phase roughly
340 matches that of unloaded AGO1 measured with the Y691E mutant [$t_{1/2}$(WT, rapid) = 1.6±0.6
341 h, $t_{1/2}$(Y691E) = 2.5±0.5 h]. We therefore repeated the pulse-labeling experiments with wild
342 type and NcGN interaction site mutants in the unloaded FLAG-AGO1^{Y691E} version, i.e.
343 FLAG-AGO1^{Y691E} vs FLAG-AGO1$^{Y691E/KKME}$. These experiments showed a modest, but
344 reproducible reduction in degradation rate of the mutant with the defective NcGN interaction
345 site (Fig. 6c,e; results of two independent experiments shown to convey their quantitative
346 variability). We conclude that intact NcGN interaction sites, including the N-coil, are
347 necessary for maximal turnover rates of unloaded AGO1 *in vivo*.
348
349 *The N-coil is uniquely accessible in unloaded AGO1*

350 The results presented thus far establish that residues in the N-coil make direct contacts to
351 the ATI1-IDR, that the ATI1-IDR can interact with the RNA-free state of AGO1, and that
352 ATI1-IDR interaction sites in the NcGN of unloaded AGO1 contribute measurably, if
353 modestly, to its rapid turnover *in vivo*. Because of the unique structural properties of the N-
354 coil, we hypothesized that this part of AGO proteins could be a site with substantially altered
355 accessibility between loaded and unloaded conformations of AGO that would allow specific
356 recognition of unloaded AGO for degradation. To test this hypothesis, we raised antibodies
357 against a 16-aa N-coil peptide (F177-C192). This polyclonal antibody specifically recognized
358 the N-coil as demonstrated by its clear reactivity towards FLAG-immuno-purified, denatured
359 AGO1 with a wild type N-coil, but substantial loss of reactivity with FLAG-AGO1 carrying the
360 K185E/K190E mutations in the N-coil (Fig. 7a,b). We next used this antibody to probe the
361 accessibility of the N-coil in AGO1 in two different ways. First, we observed that binding of
362 equal amounts of N-coil antibody required 10-fold higher amounts of immuno-purified,
363 native, immobilized FLAG-AGO1^{WT} (largely small RNA-bound) than of similarly purified
364 unloaded AGO1 (FLAG-AGO1^{Y691E}) (Fig. 7b,c). We note that this difference cannot be
365 explained by potentially different patterns of post-translational modifications in the N-coil,
366 because the antibody recognized denatured forms of the two AGO1 variants equally
367 efficiently (Fig. 7b). Second, direct immunoprecipitation from total lysates using the N-coil
368 antibody resulted in markedly more efficient recovery (~10 fold) of FLAG-AGO1^{Y691E} than of
369 FLAG-AGO1^{WT} (Fig. 7d), in contrast to the result obtained with FLAG antibodies (Fig. 7b).
370 These observations provide clear evidence that the N-coil of AGO1 is preferentially
371 accessible in the unloaded state.
372
373 *Conformational flexibility of the N-coil is widespread in eukaryotic Ago- and Piwi-clade*
374 *proteins*
375 We finally inspected existing structural data on eukaryotic AGO proteins both of the Ago and
376 Piwi clades for information on potential structural flexibility of the N-coil, if possible
377 dependent on the loading status. The structures of the human miRNA-associated Ago
378 proteins, Ago1-Ago4 in the loaded state all show the N-coil in a nearly identical conformation
379 firmly associated with the Piwi domain as depicted in Fig. 1, and are, therefore, not
380 informative in this regard. However, several regions of differential solvent exposure between
381 RNA-free and guide RNA-associated human Ago2 can be identified from recent data on

382 hydrogen-deuterium exchange rates in these two states [49] (Fig. 8a). These include the N-
383 coil and, in particular, the nearby hydrophilic environment caging the guanidium group of the
384 conserved R182 side chain in the RNA-bound state (Fig. 1a). This observation on HsAgo2
385 extends the conclusion reached here with AtAGO1 that the N-coil assumes different
386 conformations depending on the loading status of AGO.

387 In the Piwi-clade, three structures of piRNA-bound proteins are available: silkworm
388 (*Bombyx mori*) Siwi, *Drosophila melanogaster* (Dm) Piwi, and the sea sponge *Ephydatia*
389 *fluviatilis* (Ef) Piwi. The Siwi structure shows an N-coil from I130 to G148
390 (ISILRTRPEAVTSKKGTSG) associated with the MID-Piwi lobe much like in Ago-clade
391 structures, while *Ef* Piwi shows a partial and *Dm* Piwi no N-coil at all (Fig. 8b), presumably
392 due to proteolytic cleavage prior to crystallization. These indications of facultative
393 association of Piwi-clade N-coils with the MID-Piwi lobe domain suggest that the N-coil
394 exhibits conformational flexibility, perhaps accompanying conformational differences of the
395 proteins upon piRNA binding, as in the case of Ago-clade AGO proteins. Strikingly, the
396 compactness of the Piwi:piRNA complexes increases progressively from the *Dm* Piwi
397 structure (no N-coil present) to the Siwi structure (full N-coil present) (Fig. 8b,c), lending
398 support to the idea that the N-coil/MID-Piwi lobe association is an important step in reaching
399 the final conformation of mature RISC across both Piwi and Ago clades.
400

401 **Discussion**

402 *Distinction between loaded and unloaded AGO via the N-coil*

403 Our results demonstrate that the N-coil is exposed for interaction uniquely in the unloaded
404 state of AGO1. This is important, because it defines a conformational change that
405 accompanies the AGO loading process, and, thereby, confers distinct protein-protein
406 interaction properties on the two forms of AGO. Three different aspects are worth further
407 comments in this regard. First, as demonstrated here, it offers a precise molecular
408 explanation to the longstanding observation that unloaded AGO proteins in plants and
409 animals turn over much more rapidly than the small RNA-bound form. In *Arabidopsis*, this is
410 illustrated by the identification of many interactors involved in regulated proteolysis, most
411 clearly ATI1, that depend on the N-coil for interaction with the NcGN fragment of AGO1.
412 Given the structural conservation of the N-coil in widely different AGO proteins, it is likely
413 that this same molecular principle operates in many different organisms, and, thus,

414 contributes to the rapid turnover of unloaded AGO more generally. Second, because the N-
415 coil is a recurrent structural element in all AGO proteins, including the Piwi clade, its
416 exposure in unloaded forms may also explain other molecular properties distinct from rapid
417 turnover of unloaded AGO. For instance, in insect germline cells, Piwi proteins engage in a
418 so-called ping-pong amplification cycle of piRNAs derived from transposable elements.
419 Ping-pong amplification entails cleavage of a sense piRNA precursor transcript by a mature
420 piRISC containing the Piwi protein Aubergine (Aub) bound to a primary, anti-sense piRNA,
421 and subsequent loading of the sense cleavage fragment onto another Piwi-clade protein,
422 Ago3[50-52]. Ago3 is precluded from primary piRNA association by the protein Krimper that
423 associates with Ago3 specifically in the free state[53]. The definition of the molecular
424 determinants of the recognition of the unloaded state of Ago3 by Krimper remains
425 incomplete[53], but it is now an obvious possibility that the N-coil of Ago3 is one of those
426 determinants. Third, the demonstration that the N-coil becomes inaccessible to antibodies
427 after loading reveals new insight into the molecular mechanics of the loading process itself.
428 It is a reasonable interpretation of our data that attachment of the N-coil to the Piwi domain
429 is a key step in reaching the compact conformation of the loaded structure observed in
430 human Ago1-4, in particular via the salt bridge deep inside of the Piwi domain involving the
431 universally conserved R182 in the Arabidopsis AGO1 N-coil. Our inspection of available Piwi
432 protein structures lends support to this interpretation, because the compactness of the
433 structures follows the degree of N-coil/MID-Piwi association, consistent with the N-coil acting
434 as a zipper that holds the two lobes together in a compact conformation. Finally, we note
435 that our identification of Hsp90 as an interactor of the N-coil also suggests a simple
436 explanation for why chaperone interaction protects AGO proteins from rapid proteolysis. If
437 the N-coil, and potentially other structural determinants with similar exclusive exposure in
438 the unloaded state of AGO, are concealed via chaperone interaction, chaperone binding to
439 an AGO protein would preclude its interaction with the factors targeting its unloaded form
440 for proteolysis.
441
442 *Possible roles of N-coil-mediated degradation of unloaded AGO1*
443 While our study provides a clear answer to the question of how RNA-free AGO1 can be
444 specifically targeted for rapid proteolysis, it does not provide insight into the biological
445 importance of such clearance of unloaded AGO1. The most straightforward explanation for

446 the importance of rapid proteolysis of free AGO proteins is that it precludes loading of
447 illegitimate small RNA species such as degradation fragments, and thereby eliminates
448 potentially dangerous unwanted AGO-mediated gene repression and competition with *bona*
449 *fide* regulatory small RNAs. Although this explanation is plausible, it may not be the only
450 reason underlying the rapid degradation of free AGO proteins. Protection from loading of
451 endogenous RNA degradation fragments is a fundamental molecular property required in
452 the earliest ancestors in which AGO proteins are present, and the machinery responsible
453 for degradation of unloaded AGO may therefore be expected to be deeply conserved in
454 eukaryotes. However, with the exception of the histone ubiquitin ligase HUB1 and the
455 Translationally Controlled Tumor Protein (TCTP), the AGO1 NcGN interactors isolated here
456 are generally not conserved beyond plants, including proteins with roles in regulated
457 proteolysis such as ATI1 and ATI2. Which additional factors may drive the evolution of
458 systems to rapidly degrade unloaded AGOs? Since there is now evidence indicating that
459 several plant and animal pathogens, including fungi, oomycetes, parasitic plants, and
460 nematodes, use small RNAs as virulence factors [54-57], it is an attractive possibility that rapid
461 proteolysis of unloaded AGO proteins also evolved as a protective mechanism to defend
462 against those pathogens whose virulence is enhanced by reshaping host gene expression
463 using secreted siRNAs. Clearly, the identification of the N-coil as a site of protein-protein
464 interaction accessible only in RNA-free AGO should facilitate tests of this hypothesis across
465 plant and animal kingdoms.
466
467 **Figure legends**
468 **Fig. 1 | Structural properties and conserved interactions of the N-coil in Hs-Ago2.**
469 Overview of the Hs-Ago2 domain structure with surface outline of the globular N domain and
470 the N-coil. **a**, “side view”; **b**, “bottom view”. **c**, Intra-molecular interactions between the N-
471 coil and the remaining part of Hs-Ago2 as calculated by the Protein Interfaces, Surfaces and
472 Assemblies service PISA[58]. The solvation energy gain of the N-coil is calculated as the
473 difference between free energy of the associated and the dissociated N-coil. A negative
474 solvation energy, $\Delta_i G$, of a residue makes a positive contribution to the solvation energy
475 gain of the interface thus favoring the dissociated state. The color gradient (blue to red)
476 indicates the effect sizes of buried surface area and solvation energy and highlights the
477 unique properties of Arg-28. **d**, Inlet showing conserved residues and bonds between a

478 buried arginine side chain in the N-coil (R28 in Hs-Ago2) and nearby residues. Data and
479 presentations were made using the crystal structure coordinates of the miR20a-bound Hs-
480 Ago2 (PDB 4F3T)[15].
481
482 **Fig. 2 | Interactions with AGO1-NcGN are specific and often require an intact N-coil.**
483 **a**, Yeast two-hybrid analysis of ATI1 and ATI2 fused to the activation domain (AD) of the
484 yeast transcription factor Gal4 co-expressed either with NcGN domains of
485 AGO1/AGO10/AGO4 fused to the DNA binding domain of Gal4 (BD), or with Gal4-BD alone
486 (empty). 10-fold serial dilutions of yeast cells were spotted on permissive (left) and selective
487 (right) media. **b**, β-galactosidase activity measured in an *ortho*-nitrophenyl-β-galactoside
488 (ONPG) assay conducted with total protein lysates prepared from yeast strains expressing
489 each candidate fused to Gal4-AD and AGO1-NcGN-Gal4-BD, AGO1-NcGN^{G186R}-Gal4-BD,
490 or unfused Gal4-BD (empty). y-axis shows β-galactosidase activity in arbitrary units. The
491 yeast Swi2-Swi6 interaction was used as positive control, and co-expression of unfused
492 Gal4-AD and Gal4-BD was used as negative control.
493
494 **Fig. 3 | Residues required for ATI1/ATI2 interaction cluster in the N-coil and in surface-**
495 **exposed patches of the globular N-domain a**, Sequence alignments of the *Arabidopsis*
496 paralogs AGO1 and AGO10, and of orthologs of *Arabidopsis* AGO1 from plant species
497 representing major phylogenetic groups of land plants. The species chosen from the
498 different groups were as follows: Liverwort, *Marchantia polymorpha*; moss, *Ceratodon*
499 *purpureus*; lycophyte, *Selaginella moellendorfii*; fern; *Ceratopteris richardii*; gymnosperm,
500 *Pinus tabuliformis*; monocot, *Elaeis guineensis*; dicot, *Arabidopsis thaliana*. Residues
501 selected for mutational analysis are marked on the alignment. **b**, Alphafold ribbon model of
502 *Arabidopsis* AGO1 with the N-coil and N domain highlighted in rainbow colors. The residues
503 studied by mutation are presented in sticks and colored according to the effect of mutation
504 on ATI1/ATI2 interaction with AGO1-NcGN in the yeast two-hybrid assay. The underlying
505 evidence from yeast-two hybrid spotting assays is shown in Supplemental Fig. 7-8.
506
507 **Fig. 4 | The N-coil is a direct binding site for ATI1 *in vitro*. a**, SDS-PAGE of
508 heterologously expressed SUMO-AGO1-NcGN protein used for fluorescence labeling and
509 microscale thermophoresis (MST) assays. **b**, MST measurements of fluorescence intensity

510 of SUMO-AGO1 NcGN WT (left) and K178E (right) after application of a temperature
511 gradient. Fluorescence data obtained from the thermophoretic acquisition period were
512 normalized to the initial fluorescence before being fitted to a one-site binding curve with
513 increasing concentrations of ATI1-IDR. The reported binding constants (K_D) are calculated
514 with standard errors. **c**, Simple fluorescence intensity of Cys192-labeled His_6-SUMO-AGO1
515 NcGN WT (left) and K178E (right) as a function of the concentration of ATI1-IDR. **d, e**,
516 $^1H,^{15}N$-HSQC nuclear magnetic resonance spectra of 50 µM of ^{15}N-labeled AGO1 N-coil WT
517 (left, black) or K178E peptide (right, black), with 19 µM ATI1-IDR added (green with N-coil
518 WT, blue with N-coil K178E). Zooms of contour levels of residues K178 and C192 are
519 highlighted in the boxes. Minor peaks indicated with asterisks were assigned to a C-
520 terminally truncated version of the AGO1 N-coil peptide whose presence in the sample was
521 verified by MALDI-TOF mass spectrometry. **f, g**, Peak intensity plots of ^{15}N-labeled AGO1
522 N-coil peptide (50 µM) upon titration of ATI1-IDR. Peak intensities are normalized to peak
523 intensities observed with free AGO1 N-coil peptide. **h**, Peak intensity of residues K178 (for
524 the AGO1 wild type N-coil, green) and E178 (for the K178E N-coil mutant, blue) as a function
525 of the ATI1-IDR concentration. The data points were fitted to a one-site binding curve.
526
527 **Fig. 5 | Unloaded AGO1 interacts with ATI1 *in vivo*. a,** Confocal images showing results
528 of bimolecular fluorescence complementation (BiFC) assays to probe the AGO1-ATI1
529 interaction *in vivo*. The C-terminal half of YFP was fused to AGO10, or to wild type or
530 unloaded (Y691E) AGO1 with either an intact or a mutated (K185E/K190E) N-coil. The N-
531 terminal half of YFP was fused to ATI1. Both fused halves of YFP were expressed from the
532 same plasmid also expressing free RFP. For each BiFC pair, possible interaction is detected
533 by fluorescence from reconstituted YFP. RFP fluorescence serves as a control for
534 transformation. Merged channel images demonstrate the presence of yellow fluorescence
535 only in transformed cells. Scale bar, 50 µm. **b**, Quantification of YFP signal normalized to
536 RFP signal in the given number of YFP-positive cells for the interactions shown in a. Letters
537 indicate groups with statistically significantly different $\log_2$(YFP/RFP) ratios ($p < 0.05$;
538 ANOVA with post-hoc Tukey Honestly Significant Difference test). See Supplemental Fig. 9
539 for evidence that $AGO1^{Y691E}$ is unloaded, and Supplemental Fig. 10 for image data
540 underlying the quantification in b.
541

542 **Fig. 6 | An intact AGO1 N-coil is required for maximal turnover rate of unloaded AGO1**
543 ***in vivo*. a**, Ratios of normalized YFP protein to YFP mRNA levels as quantified by protein
544 and RNA blots in stable transgenic lines constitutively expressing AGO1 NcGN-YFP fusions,
545 either in WT or in the *ati1-1/ati2* knock-out background. Ratios are normalized to AGO1-
546 NcGN^{WT}-YFP expressed in WT. KKK, K178E/K185E/K190E; 6mut,
547 KKK/P259E/M304E/E307A. **b**, Kinetic model of the two different fates of newly synthesized
548 AGO1: direct degradation (κ_1), or small RNA loading (κ_2) followed by degradation (κ_3). **c**,
549 Quantification of ^{35}S-Met/Cys incorporation into FLAG-AGO1^{WT}, FLAG-AGO1^{Y691E} or FLAG-
550 AGO1$^{KKME/Y691E}$ as a function of pulse time. The lines represent a fit to an exponential
551 equation for unloadable AGO1 containing the Y691E mutation and a fit to a double
552 exponential equation for the WT AGO1. The half-lives calculated by the fitted models are
553 given in hours +/- standard deviation, as detailed in Methods. **d**, Zoom in of the dashed area
554 of **c**. **e**, Result of an independent experiment done as in **c** to verify the slower incorporation
555 kinetics in FLAG-AGO1$^{KKME/Y691E}$ compared to FLAG-AGO1^{Y691E}. See Supplemental Fig. 11
556 for protein and RNA blot data underlying Fig. 6a, and Supplemental Fig. 12 for raw data
557 underlying Fig. 6c-e.
558
559 **Fig. 7. | The N-coil is exposed to antibody binding in the unloaded state of AGO1. a**,
560 Schematic representation of the *in vitro* binding experiment shown in **b** and **c**. **b**, Protein
561 blots of identical amounts of immobilized, immuno-affinity purified FLAG-AGO1 variants
562 (WT, Y691E, KKME/Y691E) incubated with the indicated concentrations of AGO1 N-coil
563 antibody (α-AGO1-N) and competitively eluted after extensive washing. Top panel,
564 detection with FLAG antibodies (α-FLAG) to document equal amounts of FLAG-AGO1
565 variants in each of the binding assays. Middle panel, detection with α-AGO1-N to document
566 specificity of the antibody (compare AGO1^{Y691E} (intact N-coil) to AGO1$^{Y691E/}$KKME (two point
567 mutations in N-coil) and equal reactivity towards loaded and unloaded AGO1 in the
568 denatured state. Bottom panel, detection with anti-rabbit IgG to quantify the amount of α-
569 AGO1-N retained by the immobilized FLAG-AGO1 variants. **c**, Quantification of the amount
570 of α-Rabbit IgG signal in b at different α-AGO1-N concentrations. The lines show an
571 exponential fit to the data. **d**, Immunoprecipitation of FLAG-AGO1^{WT} and FLAG-AGO^{Y691E}
572 with α-AGO1-N antibody from total lysates of plants expressing comparable levels of FLAG-

573 AGO1^{WT} and FLAG-AGO^{Y691E}. The Ponceau stain of the lanes containing aliquots of total
574 lysates shows a crop around the large subunit of RuBisCO.
575
576 **Fig 8. | Structural properties, including flexibility, of the N-coil are recurrent in Ago**
577 **and Piwi-clade proteins**
578 **a,** Projection onto the hAgo2 model of the fractional differential hydrogen-deuterium
579 exchange (HDX) data reported by Bibel et al. between unloaded and guide loaded hAgo2[49].
580 Increasing differences in exchange rate are indicated with progressively darker purple
581 shading. All regions with differential rates of exchange between unloaded and guide-loaded
582 hAgo2 show higher exchange rate in the unloaded state, most notably areas buried by the
583 N-coil and engaging in interactions with N-coil residue Arg28 in the guide-loaded hAgo2. **b**,
584 Structural overview of Siwi and Piwi outlining in pink their N-coils. The *Ephydatia fluviatilis*
585 and *Drosophila melanogaster* Piwi proteins harbour N-coil truncations, probably generated
586 by proteolysis during sample preparation for structural studies. **c**, Secondary structure
587 matching of the *B. mori* and *D. melanogaster* Piwi domains reveals a more relaxed state of
588 the *D. melanogaster* Piwi molecule (green) in which the structurally fixed N-coil seen in *B.*
589 *mori* Siwi is absent.
590
591
592 **References**
593

594 1. Meister, G. Argonaute proteins: functional insights and emerging roles. *Nat Rev*
595 *Genet* **14**, 447-59 (2013).
596 2. Czech, B. et al. piRNA-Guided Genome Defense: From Biogenesis to Silencing.
597 *Annual Review of Genetics* **52**, 131-157 (2018).
598 3. Bartel, D.P. Metazoan MicroRNAs. *Cell* **173**, 20-51 (2018).
599 4. Ding, S.W. & Voinnet, O. Antiviral immunity directed by small RNAs. *Cell* **130**, 413-
600 26 (2007).
601 5. Matzke, M.A. & Mosher, R.A. RNA-directed DNA methylation: an epigenetic pathway
602 of increasing complexity. *Nature reviews. Genetics* **15**, 394-408 (2014).
603 6. Poulsen, C., Vaucheret, H. & Brodersen, P. Lessons on RNA silencing mechanisms
604 in plants from eukaryotic argonaute structures. *Plant Cell* **25**, 22-37 (2013).
605 7. Qu, F., Ye, X. & Morris, J.T. Arabidopsis DRB4, AGO1, AGO7, and RDR6 participate
606 in a DCL4-initiated antiviral RNA silencing pathway negatively regulated by DCL1
607 *Proc Natl Acad Sci U S A* **105**, 14732-14737 (2008).
608 8. Jaubert, M., Bhattacharjee, S., Mello, A.F., Perry, K.L. & Moffett, P. ARGONAUTE2
609 mediates RNA-silencing antiviral defenses against Potato virus X in Arabidopsis.
610 *Plant Physiol* **156**, 1556-64 (2011).

611 9. Wang, X.B. et al. The 21-nucleotide, but not 22-nucleotide, viral secondary small
612 interfering RNAs direct potent antiviral defense by two cooperative argonautes in
613 Arabidopsis thaliana. *Plant Cell* **23**, 1625-38 (2011).
614 10. Carbonell, A. et al. Functional analysis of three Arabidopsis ARGONAUTES using
615 slicer-defective mutants. *Plant Cell* **24**, 3613-29 (2012).
616 11. Brosseau, C. & Moffett, P. Functional and Genetic Analysis Identify a Role for
617 Arabidopsis ARGONAUTE5 in Antiviral RNA Silencing. *The Plant Cell* **27**, 1742-1754
618 (2015).
619 12. Wang, Y., Sheng, G., Juranek, S., Tuschl, T. & Patel, D.J. Structure of the guide-
620 strand-containing argonaute silencing complex. *Nature* (2008).
621 13. Schirle, N.T. & MacRae, I.J. The crystal structure of human Argonaute2. *Science* **336**,
622 1037-40 (2012).
623 14. Nakanishi, K., Weinberg, D.E., Bartel, D.P. & Patel, D.J. Structure of yeast Argonaute
624 with guide RNA. *Nature* **486**, 368-74 (2012).
625 15. Elkayam, E. et al. The structure of human argonaute-2 in complex with miR-20a. *Cell*
626 **150**, 100-10 (2012).
627 16. Ma, J.B. et al. Structural basis for 5'-end-specific recognition of guide RNA by the A.
628 fulgidus Piwi protein. *Nature* **434**, 666-70 (2005).
629 17. Parker, J.S., Roe, S.M. & Barford, D. Structural insights into mRNA recognition from
630 a PIWI domain–siRNA guide complex. *Nature* **434**, 663-666 (2005).
631 18. Ma, J.B., Ye, K. & Patel, D.J. Structural basis for overhang-specific small interfering
632 RNA recognition by the PAZ domain. *Nature* **429**, 318-22 (2004).
633 19. Iki, T. et al. In vitro assembly of plant RNA-induced silencing complexes facilitated by
634 molecular chaperone HSP90. *Mol Cell* **39**, 282-91 (2010).
635 20. Iwasaki, S. et al. Hsc70/Hsp90 chaperone machinery mediates ATP-dependent RISC
636 loading of small RNA duplexes. *Mol Cell* **39**, 292-9 (2010).
637 21. Miyoshi, T., Takeuchi, A., Siomi, H. & Siomi, M.C. A direct role for Hsp90 in pre-RISC
638 formation in Drosophila. *Nat Struct Mol Biol* **17**, 1024-6 (2010).
639 22. Iki, T., Yoshikawa, M., Meshi, T. & Ishikawa, M. Cyclophilin 40 facilitates HSP90-
640 mediated RISC assembly in plants. *EMBO J* **31**, 267-78 (2012).
641 23. Iwasaki, S. et al. Defining fundamental steps in the assembly of the Drosophila RNAi
642 enzyme complex. *Nature* (2015).
643 24. Matranga, C., Tomari, Y., Shin, C., Bartel, D.P. & Zamore, P.D. Passenger-strand
644 cleavage facilitates assembly of siRNA into Ago2-containing RNAi enzyme
645 complexes. *Cell* **123**, 607-20 (2005).
646 25. Rand, T.A., Petersen, S., Du, F. & Wang, X. Argonaute2 Cleaves the Anti-Guide
647 Strand of siRNA during RISC Activation. *Cell* **123**, 621-629 (2005).
648 26. Leuschner, P.J.F., Ameres, S.L., Kueng, S. & Martinez, J. Cleavage of the siRNA
649 passenger strand during RISC assembly in human cells. *EMBO reports* **7**, 314-320
650 (2006).
651 27. Endo, Y., Iwakawa, H.-o. & Tomari, Y. Arabidopsis ARGONAUTE7 selects miR390
652 through multiple checkpoints during RISC assembly. *EMBO reports* **14**, 652-658
653 (2013).
654 28. Reichholf, B. et al. Time-Resolved Small RNA Sequencing Unravels the Molecular
655 Principles of MicroRNA Homeostasis. *Mol Cell* **75**, 756-768 e7 (2019).
656 29. Derrien, B. et al. Degradation of the antiviral component ARGONAUTE1 by the
657 autophagy pathway. *Proc Natl Acad Sci U S A* **109**, 15942-6 (2012).

30. Smibert, P., Yang, J.-S., Azzam, G., Liu, J.-L. & Lai, E.C. Homeostatic control of Argonaute stability by microRNA availability. *Nature Structural & Molecular Biology* **20**, 789-795 (2013).
31. Martinez, N.J. & Gregory, R.I. Argonaute2 expression is post-transcriptionally coupled to microRNA abundance. *RNA* **19**, 605-612 (2013).
32. Johnston, M., Geoffroy, M.-C., Sobala, A., Hay, R. & Hutvagner, G. HSP90 Protein Stabilizes Unloaded Argonaute Complexes and Microscopic P-bodies in Human Cells. *Molecular Biology of the Cell* **21**, 1462-1469 (2010).
33. Gibbings, D. et al. Selective autophagy degrades DICER and AGO2 and regulates miRNA activity. *Nat Cell Biol* **14**, 1314-21 (2012).
34. Kobayashi, H., Shoji, K., Kiyokawa, K., Negishi, L. & Tomari, Y. VCP Machinery Mediates Autophagic Degradation of Empty Argonaute. *Cell Reports* **28**, 1144-1153.e4 (2019).
35. Kobayashi, H., Shoji, K., Kiyokawa, K., Negishi, L. & Tomari, Y. Iruka Eliminates Dysfunctional Argonaute by Selective Ubiquitination of Its Empty State. *Molecular Cell* **73**, 119-129.e5 (2019).
36. Hacquard, T. et al. The Arabidopsis F-box protein FBW2 targets AGO1 for degradation to prevent spurious loading of illegitimate small RNA. *Cell Reports* **39**(2022).
37. Gregory, B.D. et al. A link between RNA metabolism and silencing affecting Arabidopsis development. *Dev Cell* **14**, 854-66 (2008).
38. Brodersen, P. et al. Isoprenoid biosynthesis is required for miRNA function and affects membrane association of ARGONAUTE 1 in Arabidopsis. *Proc Natl Acad Sci U S A* **109**, 1778-83 (2012).
39. Fang, X., Cui, Y., Li, Y. & Qi, Y. Transcription and processing of primary microRNAs are coupled by Elongator complex in Arabidopsis. *Nature Plants* **1**, 15075 (2015).
40. Hauptmann, J. et al. Turning catalytically inactive human Argonaute proteins into active slicer enzymes. *Nature Structural & Molecular Biology* **20**, 814-817 (2013).
41. Honig, A., Avin-Wittenberg, T., Ufaz, S. & Galili, G. A new type of compartment, defined by plant-specific Atg8-interacting proteins, is induced upon exposure of Arabidopsis plants to carbon starvation. *Plant Cell* **24**, 288-303 (2012).
42. Sjøgaard, I.M.Z. et al. The transmembrane autophagy cargo receptors ATI1 and ATI2 interact with ATG8 through intrinsically disordered regions with distinct biophysical properties. *Biochemical Journal* **476**, 449-465 (2019).
43. Michaeli, S. et al. The viral F-box protein P0 induces an ER-derived autophagy degradation pathway for the clearance of membrane-bound AGO1. *Proceedings of the National Academy of Sciences* **116**, 22872-22883 (2019).
44. Petersen, N.H.T. et al. Identification of proteins interacting with Arabidopsis ACD11. *Journal of Plant Physiology* **166**, 661-666 (2009).
45. Craxton, M. Evolutionary genomics of plant genes encoding N-terminal-TM-C2 domain proteins and the similar FAM62 genes and synaptotagmin genes of metazoans. *BMC Genomics* **8**, 259 (2007).
46. Rudel, S. et al. Phosphorylation of human Argonaute proteins affects small RNA binding. *Nucleic Acids Res* **39**, 2330-43 (2011).
47. Li, S. et al. MicroRNAs inhibit the translation of target mRNAs on the endoplasmic reticulum in Arabidopsis. *Cell* **153**, 562-74 (2013).

48. Sjögren, L. et al. Farnesylated heat shock protein 40 is a component of membrane-bound RISC in Arabidopsis. *Journal of Biological Chemistry* **293**, 16608-16622 (2018).
49. Bibel, B., Elkayam, E., Silletti, S., Komives, E.A. & Joshua-Tor, L. Target binding triggers hierarchical phosphorylation of human Argonaute-2 to promote target release. *eLife* **11**, e76908 (2022).
50. Brennecke, J. et al. Discrete small RNA-generating loci as master regulators of transposon activity in Drosophila. *Cell* **128**, 1089-103 (2007).
51. Gunawardane, L.S. et al. A slicer-mediated mechanism for repeat-associated siRNA 5' end formation in Drosophila. *Science* **315**, 1587-90 (2007).
52. Brennecke, J. et al. An Epigenetic Role for Maternally Inherited piRNAs in Transposon Silencing. *Science* **322**, 1387-1392 (2008).
53. Sato, K. et al. Krimper Enforces an Antisense Bias on piRNA Pools by Binding AGO3 in the Drosophila Germline. *Molecular Cell* **59**, 553-563 (2015).
54. Weiberg, A. et al. Fungal small RNAs suppress plant immunity by hijacking host RNA interference pathways. *Science* **342**, 118-23 (2013).
55. Hou, Y. et al. A Phytophthora Effector Suppresses Trans-Kingdom RNAi to Promote Disease Susceptibility. *Cell Host & Microbe* **25**, 153-165.e5 (2019).
56. Shahid, S. et al. MicroRNAs from the parasitic plant Cuscuta campestris target host messenger RNAs. *Nature* **553**, 82-85 (2018).
57. Buck, A.H. et al. Exosomes secreted by nematode parasites transfer small RNAs to mammalian cells and modulate innate immunity. *Nature Communications* **5**, 5488 (2014).
58. Krissinel, E. & Henrick, K. Inference of Macromolecular Assemblies from Crystalline State. *Journal of Molecular Biology* **372**, 774-797 (2007).

On-line content

Methods, Supplemental Figures 1-13, Supplemental Tables 1-2, additional references supporting Methods and legends of supplemental figures and tables.

Data availability

NMR data have been deposited at the Biological Magnetic Resonance Bank (BMRB) under BMRB entry 51660.

Code availability

The study did not develop new code. Standard procedures for mathematical and statistical analysis of data are described in Methods.

745 **Acknowledgements**
746 Theo Bølsterli and his team are thanked for plant care and Signe A. Sjørup for assistance
747 with MALDI-TOF experiments and purification of proteins. We thank Laura Arribas-
748 Hernández and Diego López-Marquez for critical reading of the manuscript.
749
750 **Funding**
751 This work was supported by a Hallas Møller Stipend (Hallas Møller 2010) and a project grant
752 (NNF17OC0029194) from the Novo Nordisk Foundation, and Starting (ERC-2011-StG
753 282460 MICROMECCA) and Consolidator Grants (ERC-2016-CoG 726417 PATHORISC)
754 from the European Research Council, all to PB. The work was also supported by the Novo
755 Nordisk Foundation Challenge program (REPIN; grant number NNF18OC0033926 to BBK).
756 The NMR spectra were recorded at cOpenNMR, an infrastructure initiative supported by the
757 Novo Nordisk Foundation grant number NNF18OC0032996.
758
759 **Author contributions**
760 SB constructed plant lines expressing unloaded FLAG-AGO1 and its combinations with N-
761 coil mutants in *ago1-3* knockout backgrounds, conducted bimolecular fluorescence
762 complementation analyses, pulse-labeling experiments and resulting data analysis,
763 developed the AGO1 N-coil antibody and conducted binding experiments and subsequent
764 data analysis. IMZB expressed and purified recombinant proteins, conducted MST assays
765 with SB and NMR experiments with AP, developed the ATI1 antibody, and participated with
766 SB in preliminary tests and AGO1 binding experiments with a lower-affinity N-coil antibody
767 not used in the final experiments reported here. SK conducted two-hybrid screening and
768 initial mutational analysis of AGO1 NcGN, further developed by AM. EDO set up CRISPR-
769 Cas9 engineering, isolated *ati2* mutant alleles in Col-0, constructed *ati1/ati2* double mutants,
770 and some transgenic lines expressing N-coil mutants of AGO1 in *ago1-3* knockout
771 backgrounds. CP conducted analysis of structures and suggested that the N-coil may adopt
772 conformations different from the one seen in crystal structures of HsAgo2. BBK helped
773 design NMR experiments, and, together with AP, supervised all work and data analysis
774 related to those experiments. PB designed and supervised the study and wrote the
775 manuscript with contributions from all authors.
776

Competing interests

The authors declare no competing interests.

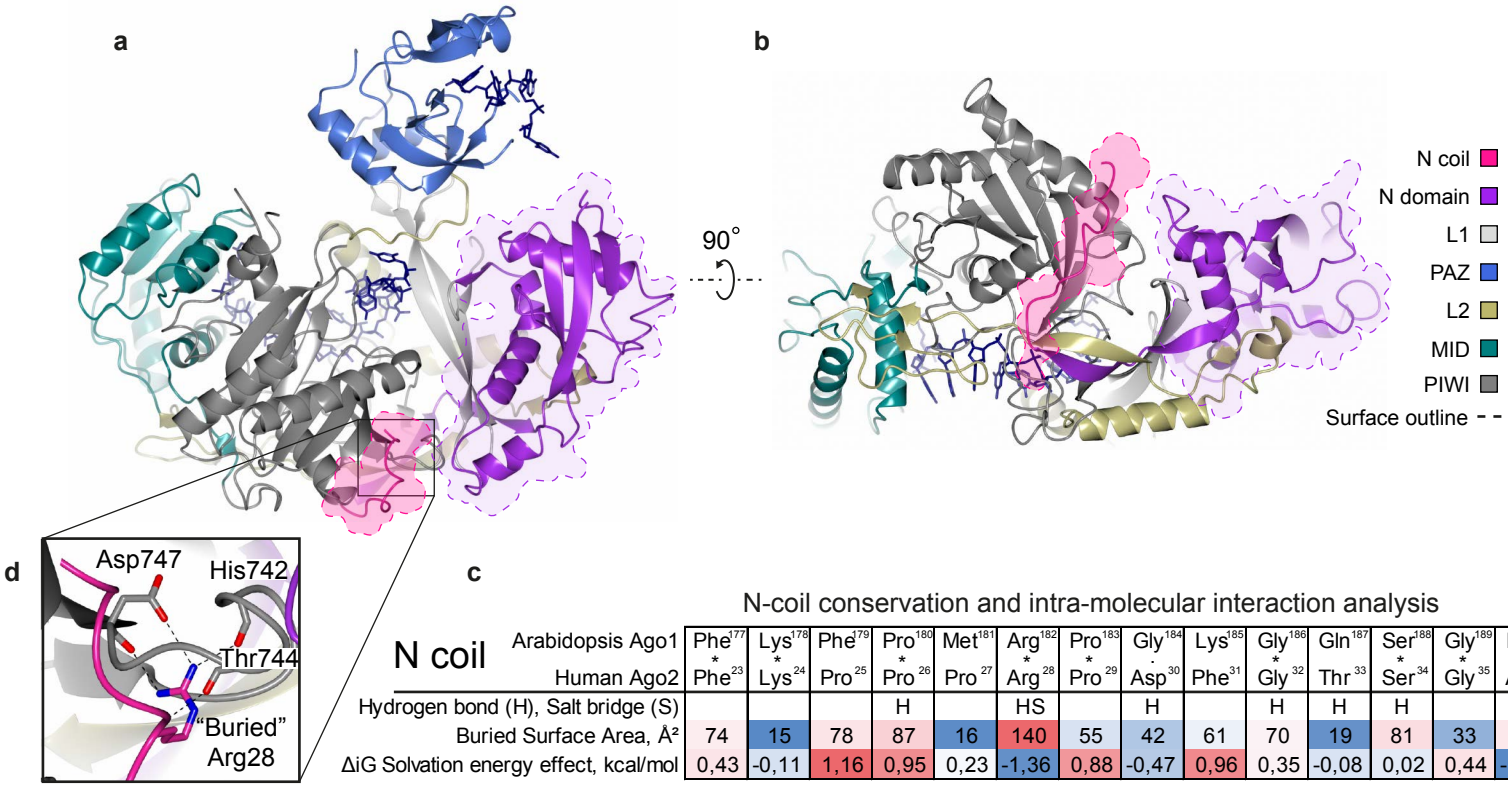

N coil														
Arabidopsis Ago1	Phe[177]	Lys[178]	Phe[179]	Pro[180]	Met[181]	Arg[182]	Pro[183]	Gly[184]	Lys[185]	Gly[186]	Gln[187]	Ser[188]	Gly[189]	Lys[190]
	*	*		*		*	*	.		*		*	*	.
Human Ago2	Phe[23]	Lys[24]	Pro[25]	Pro[26]	Pro[27]	Arg[28]	Pro[29]	Asp[30]	Phe[31]	Gly[32]	Thr[33]	Ser[34]	Gly[35]	Arg[36]
Hydrogen bond (H), Salt bridge (S)				H		HS		H		H	H	H		HS
Buried Surface Area, Å²	74	15	78	87	16	140	55	42	61	70	19	81	33	76
ΔiG Solvation energy effect, kcal/mol	0,43	-0,11	1,16	0,95	0,23	-1,36	0,88	-0,47	0,96	0,35	-0,08	0,02	0,44	-1,48

Fig. 1 | Structural properties and conserved interactions of the N-coil in Hs-Ago2. Overview of the Hs-Ago2 domain structure with surface outline of the globular N domain and the N-coil. **a**, "side view"; **b**, "bottom view". **c**, Intra-molecular interactions between the N-coil and the remaining part of Hs-Ago2 as calculated by the Protein Interfaces, Surfaces and Assemblies service PISA[58]. The solvation energy gain of the N-coil is calculated as the difference between free energy of the associated and the dissociated N-coil. A negative solvation energy, $\Delta_i G$, of a residue makes a positive contribution to the solvation energy gain of the interface thus favoring the dissociated state. The color gradient (blue to red) indicates the effect sizes of buried surface area and solvation energy and highlights the unique properties of Arg-28. **d**, Inlet showing conserved residues and bonds between a buried arginine side chain in the N-coil (R28 in Hs-Ago2) and nearby residues. Data and presentations were made using the crystal structure coordinates of the miR20a-bound Hs-Ago2 (PDB 4F3T)[15].

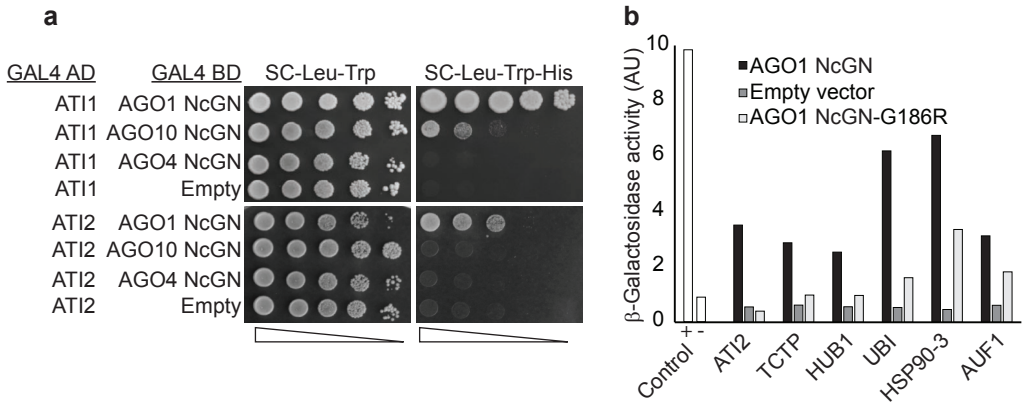

Fig. 2 | Interactions with AGO1-NcGN are specific and often require an intact N-coil. a, Yeast two-hybrid analysis of ATI1 and ATI2 fused to the activation domain (AD) of the yeast transcription factor Gal4 co-expressed either with NcGN domains of AGO1/AGO10/AGO4 fused to the DNA binding domain of Gal4 (BD), or with Gal4-BD alone (empty). 10-fold serial dilutions of yeast cells were spotted on permissive (left) and selective (right) media. **b**, β-galactosidase activity measured in an *ortho*-nitrophenyl-β-galactoside (ONPG) assay conducted with total protein lysates prepared from yeast strains expressing each candidate fused to Gal4-AD and AGO1-NcGN-Gal4-BD, AGO1-NcGN^{G186R}-Gal4-BD, or unfused Gal4-BD (empty). y-axis shows β-galactosidase activity in arbitrary units. The yeast Swi2-Swi6 interaction was used as positive control, and co-expression of unfused Gal4-AD and Gal4-BD was used as negative control.

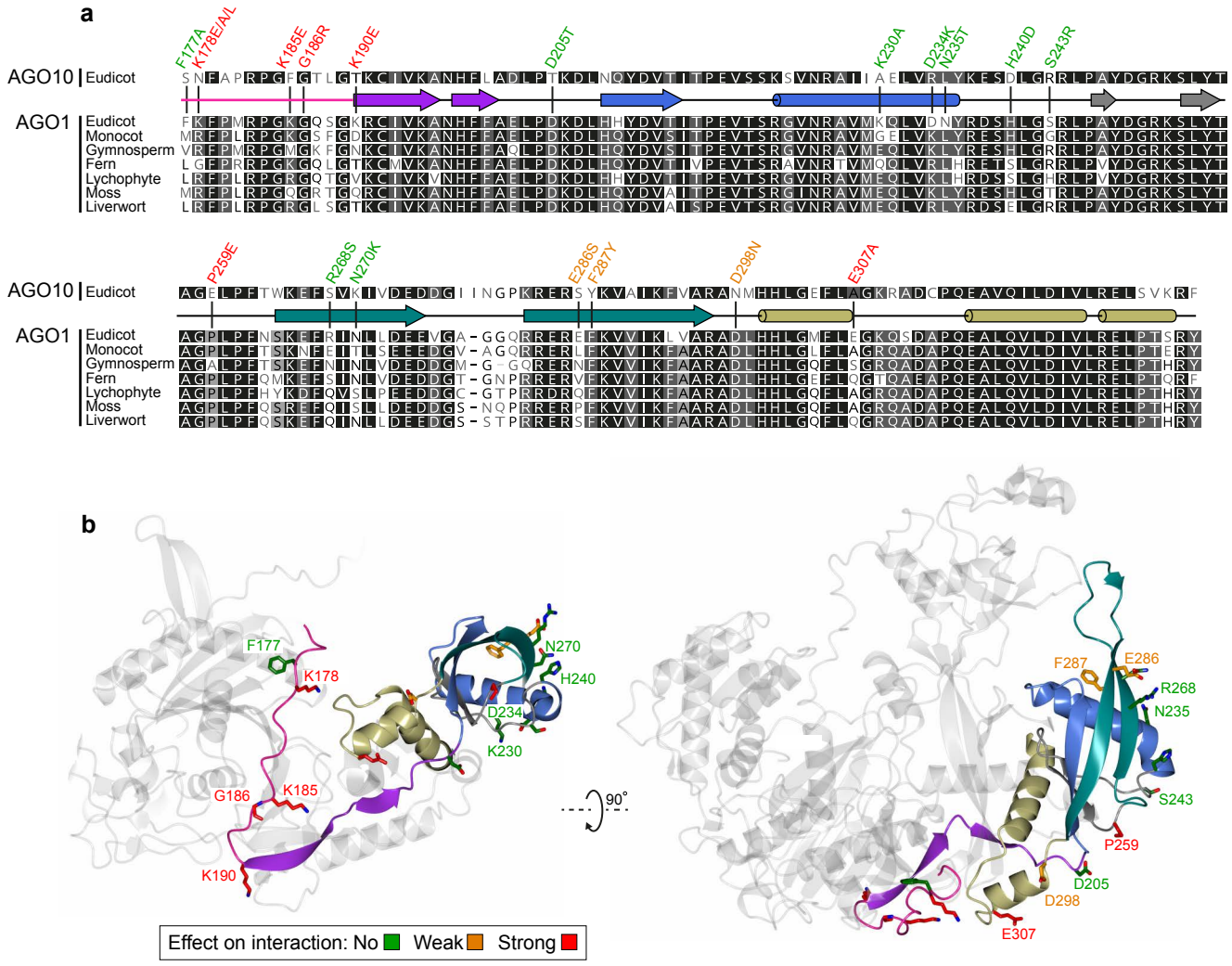

Fig. 3 | Residues required for ATI1/ATI2 interaction cluster in the N-coil and in surface-exposed patches of the globular N-domain. a, Sequence alignments of the *Arabidopsis* paralogs AGO1 and AGO10, and of orthologs of *Arabidopsis* AGO1 from plant species representing major phylogenetic groups of land plants. The species chosen from the different groups were as follows: Liverwort, *Marchantia polymorpha*; moss, *Ceratodon purpureus*; lycophyte, *Selaginella moellendorfii*; fern; *Ceratopteris richardii*; gymnosperm, *Pinus tabuliformis*; monocot, *Elaeis guineensis*; dicot, *Arabidopsis thaliana*. Residues selected for mutational analysis are marked on the alignment. **b**, Alphafold ribbon model of *Arabidopsis* AGO1 with the N-coil and N domain highlighted in rainbow colors. The residues studied by mutation are presented in sticks and colored according to the effect of mutation on ATI1/ATI2 interaction with AGO1-NcGN in the yeast two-hybrid assay. The underlying evidence from yeast-two hybrid spotting assays is shown in Supplemental Fig. 7-8.

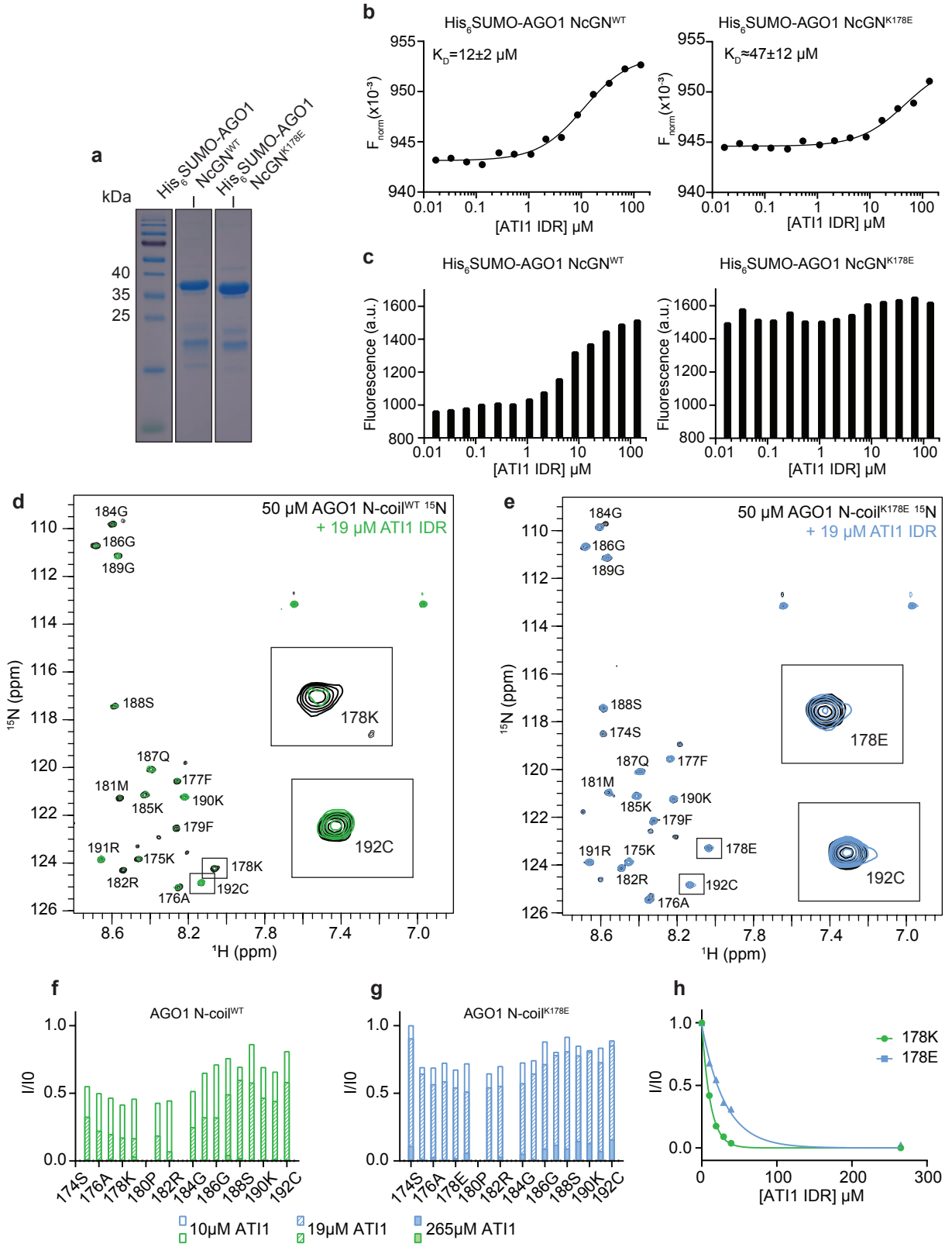

Fig. 4 | The N-coil is a direct binding site for ATI1 *in vitro*. **a**, SDS-PAGE of heterologously expressed His_6SUMO-AGO1-NcGN protein used for fluorescence labeling and microscale thermophoresis (MST) assays. **b**, MST measurements of fluorescence intensity of His_6SUMO-AGO1 NcGN WT (left) and K178E (right) after application of a temperature gradient. Fluorescence data obtained from the thermophoretic acquisition period were normalized to the initial fluorescence before being fitted to a one-site binding curve with increasing concentrations of ATI1-IDR. The reported binding constants (K_D) are calculated with standard errors. **c**, Simple fluorescence intensity of Cys192-labeled His_6SUMO-AGO1 NcGN WT (left) and K178E (right) as a function of the concentration of ATI1-IDR. **d, e**, ^{1}H,^{15}N-HSQC nuclear magnetic resonance spectra of 50 μM of ^{15}N-labeled AGO1 N-coil WT (left, black) or K178E peptide (right, black), with 19 μM ATI1-IDR added (green with N-coil WT, blue with N-coil K178E). Zooms of contour levels of residues K178 and C192 are highlighted in the boxes. Minor peaks were assigned to a C-terminally truncated version of the AGO1 N-coil peptide whose presence in the sample was verified by MALDI-TOF mass spectrometry. **f, g**, Peak intensity plots of ^{15}N-labeled AGO1 N-coil peptide (50 μM) upon titration of ATI1-IDR. Peak intensities are normalized to peak intensities observed with free AGO1 N-coil peptide. **h**, Peak intensity of residues K178 (for the AGO1 wild type N-coil, green) and E178 (for the K178E N-coil mutant, blue) as a function of the ATI1-IDR concentration. The data points are fitted to an exponential function.

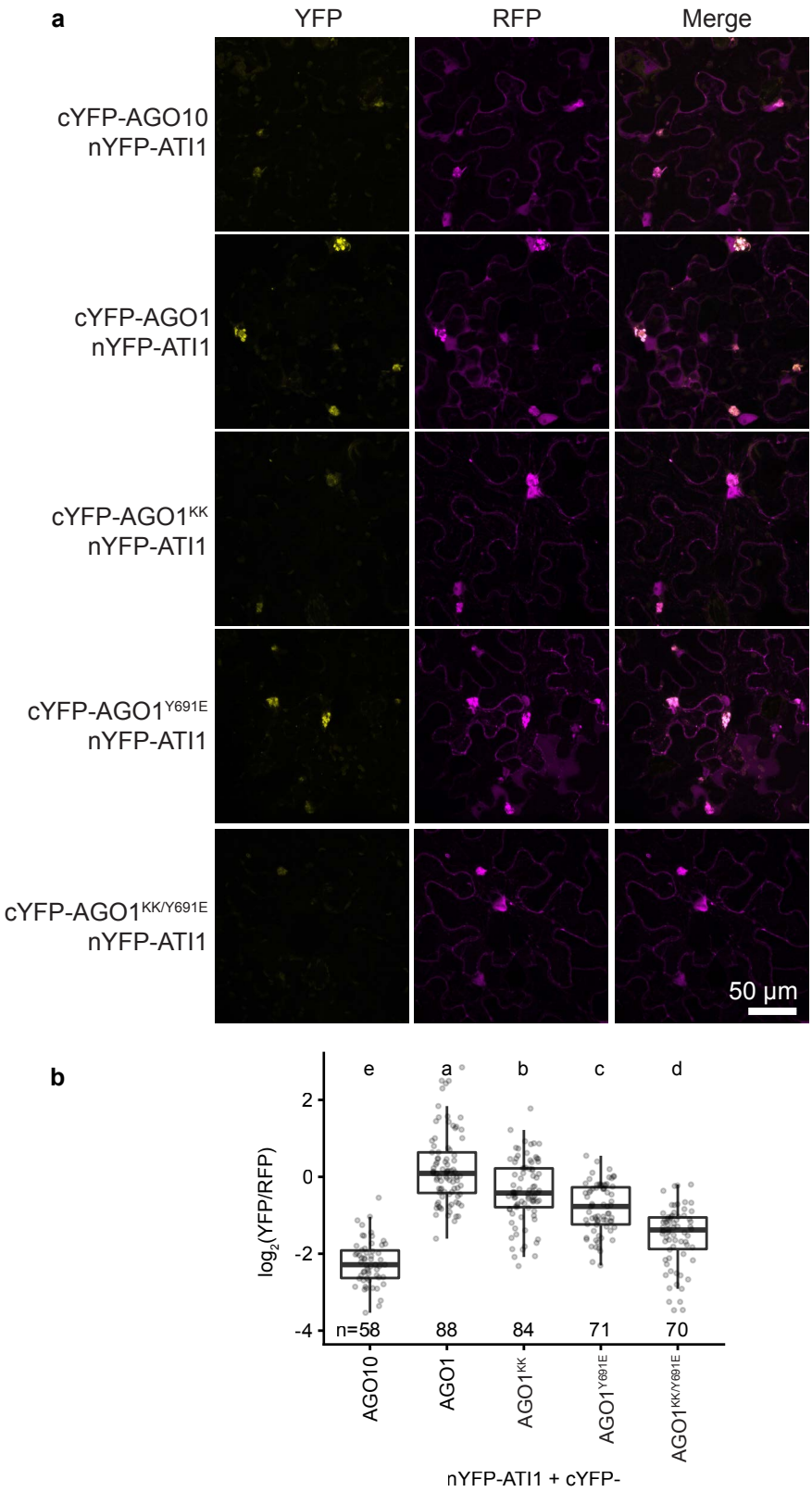

Fig. 5 | Unloaded AGO1 interacts with ATI1 *in vivo*. a, Confocal images showing results of bimolecular fluorescence complementation (BiFC) assays to probe the AGO1-ATI1 interaction *in vivo*. The C-terminal half of YFP was fused to AGO10, or to wild type or unloaded (Y691E) AGO1 with either an intact or a mutated (K185E/K190E) N-coil. The N-terminal half of YFP was fused to ATI1. Both fused halves of YFP were expressed from the same plasmid also expressing free RFP. For each BiFC pair, possible interaction is detected by fluorescence from reconstituted YFP. RFP fluorescence serves as a control for transformation. Merged channel images demonstrate the presence of yellow fluorescence only in transformed cells. Scale bar, 50 µm. **b**, Quantification of YFP signal normalized to RFP signal in the given number of YFP-positive cells for the interactions shown in a. Letters indicate groups with statistically significantly different $\log_2$(YFP/RFP) ratios ($p < 0.05$; ANOVA with post-hoc Tukey Honestly Significant Difference test). See Supplemental Fig. 9 for evidence that AGO1^{Y691E} is unloaded, and Supplemental Fig. 10 for image data underlying the quantification in b. KK, K185E/K190E.

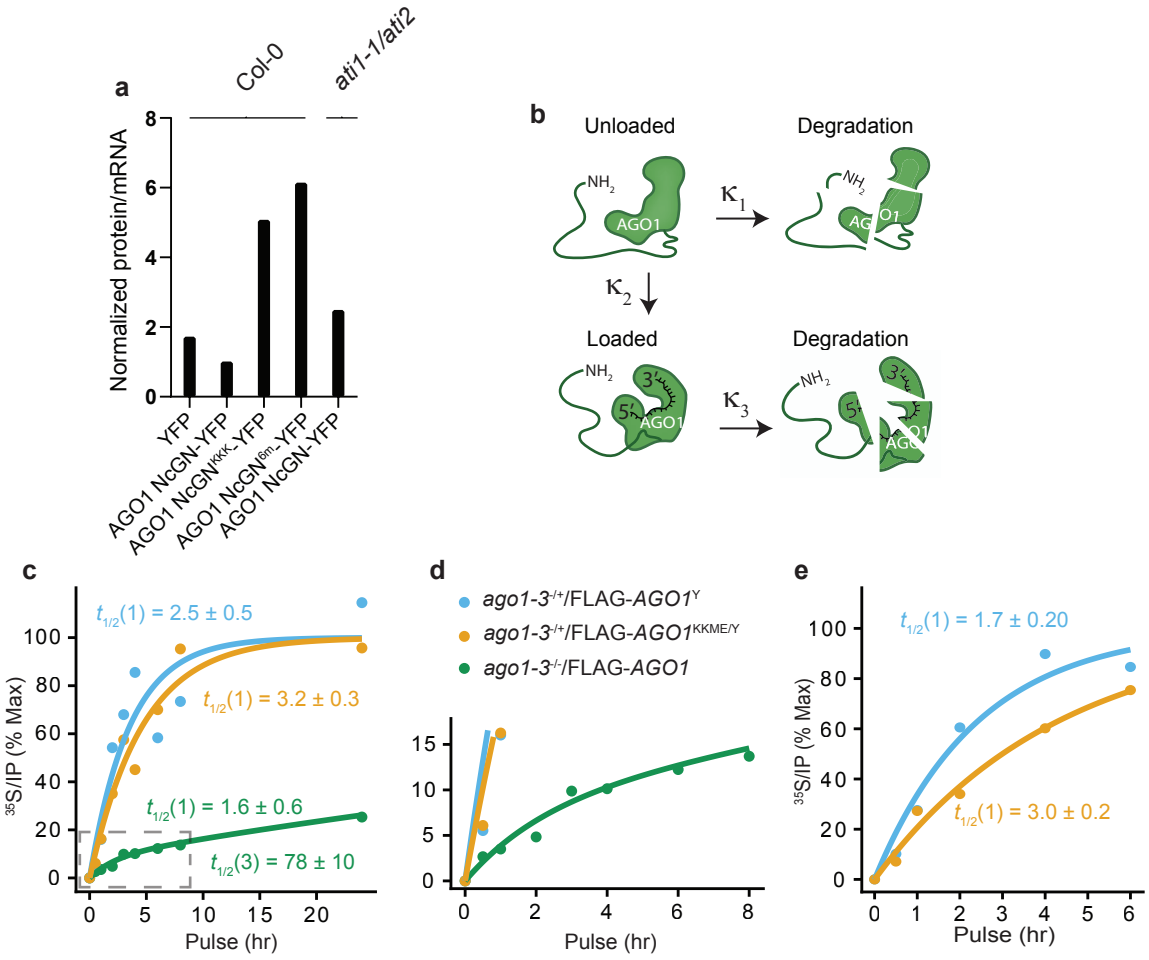

Fig. 6 | An intact AGO1 N-coil is required for maximal turnover rate of unloaded AGO1 *in vivo*. **a**, Ratios of normalized YFP protein to YFP mRNA levels as quantified by protein and RNA blots in stable transgenic lines constitutively expressing AGO1 NcGN-YFP fusions, either in WT or in the *ati1-1/ati2* knock-out background. Ratios are normalized to AGO1-NcGN^{WT}-YFP expressed in WT. KKK, K178E/K185E/K190E; 6mut, KKK/P259E/M304E/E307A. **b**, Kinetic model of the two different fates of newly synthesized AGO1: direct degradation (κ_1), or small RNA loading (κ_2) followed by degradation (κ_3). **c**, Quantification of ^{35}S-Met/Cys incorporation into FLAG-AGO1^{WT}, FLAG-AGO1^{Y691E} or FLAG-AGO1$^{KKME/Y691E}$ as a function of pulse time. The lines represent a fit to an exponential equation for unloadable AGO1 containing the Y691E mutation and a fit to a double exponential equation for the WT AGO1. The half-lives calculated by the fitted models are given in hours +/- standard deviation, as detailed in Methods. **d**, Zoom in of the dashed area of **c**. **e**, Result of an independent experiment done as in **c** to verify the slower incorporation kinetics in FLAG-AGO1$^{KKME/Y691E}$ compared to FLAG-AGO1^{Y691E}. See Supplemental Fig. 11 for protein and RNA blot data underlying Fig. 6a, and Supplemental Fig. 12 for raw data underlying Fig. 6c-e.

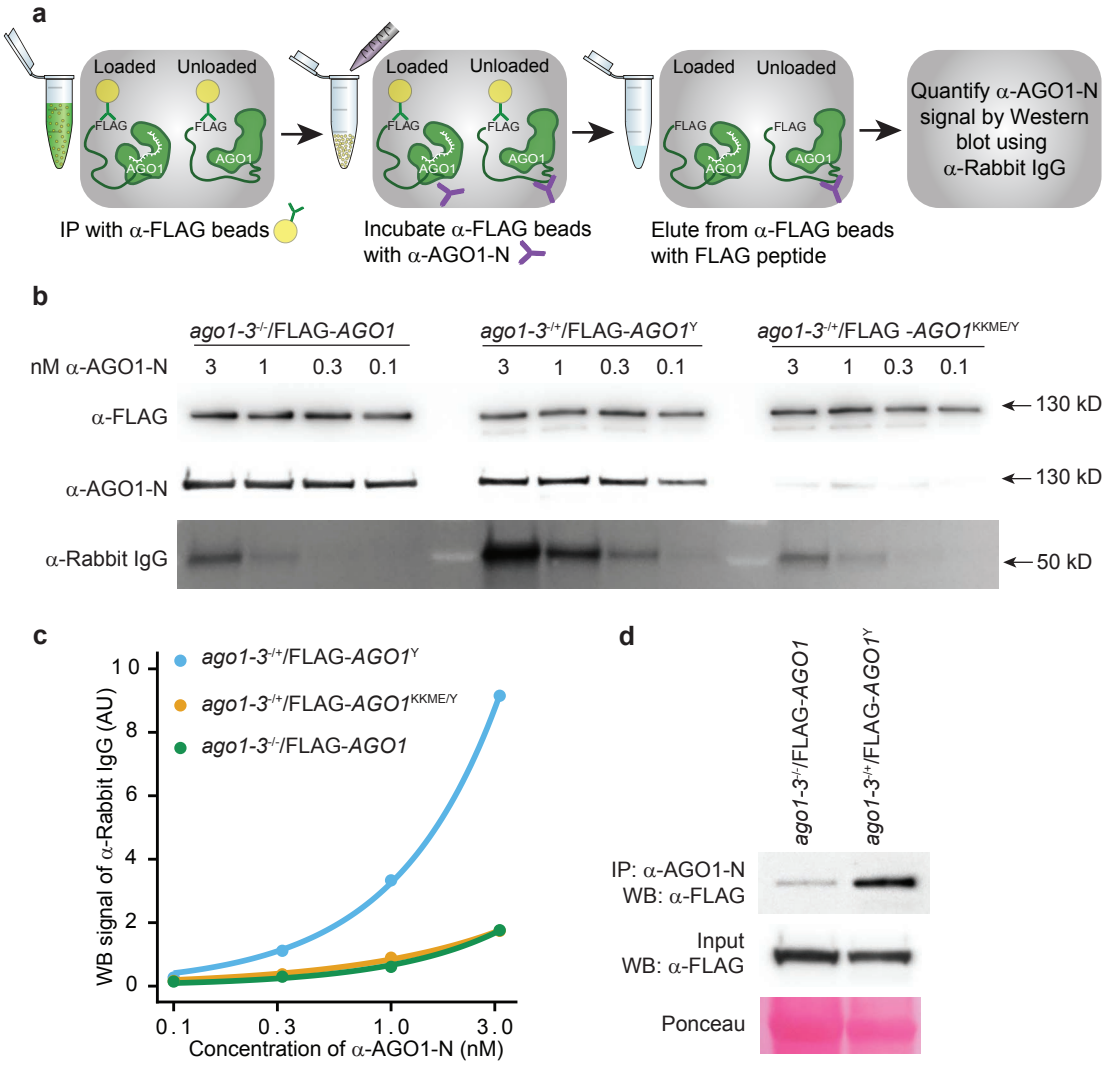

Fig. 7. | The N-coil is exposed to antibody binding in the unloaded state of AGO1. **a**, Schematic representation of the *in vitro* binding experiment shown in **b** and **c**. **b**, Protein blots of identical amounts of immobilized, immuno-affinity purified FLAG-AGO1 variants (WT, Y691E, KKME/Y691E) incubated with the indicated concentrations of AGO1 N-coil antibody (α-AGO1-N) and competitively eluted after extensive washing. Top panel, detection with FLAG antibodies (α-FLAG) to document equal amounts of FLAG-AGO1 variants in each of the binding assays. Middle panel, detection with α-AGO1-N to document specificity of the antibody (compare AGO1^{Y691E} (intact N-coil) to AGO1$^{Y691E/}$KKME (two point mutations in N-coil) and equal reactivity towards loaded and unloaded AGO1 in the denatured state. Bottom panel, detection with anti-rabbit IgG to quantify the amount of α-AGO1-N retained by the immobilized FLAG-AGO1 variants. **c**, Quantification of the amount of α-Rabbit IgG signal in b at different α-AGO1-N concentrations. The lines show an exponential fit to the data. **d**, Immunoprecipitation of FLAG-AGO1^{WT} and FLAG-AGO^{Y691E} with α-AGO1-N antibody from total lysates of plants expressing comparable levels of FLAG-AGO1^{WT} and FLAG-AGO^{Y691E}. The Ponceau stain of the lanes containing aliquots of total lysates shows a crop around the large subunit of RuBisCO.

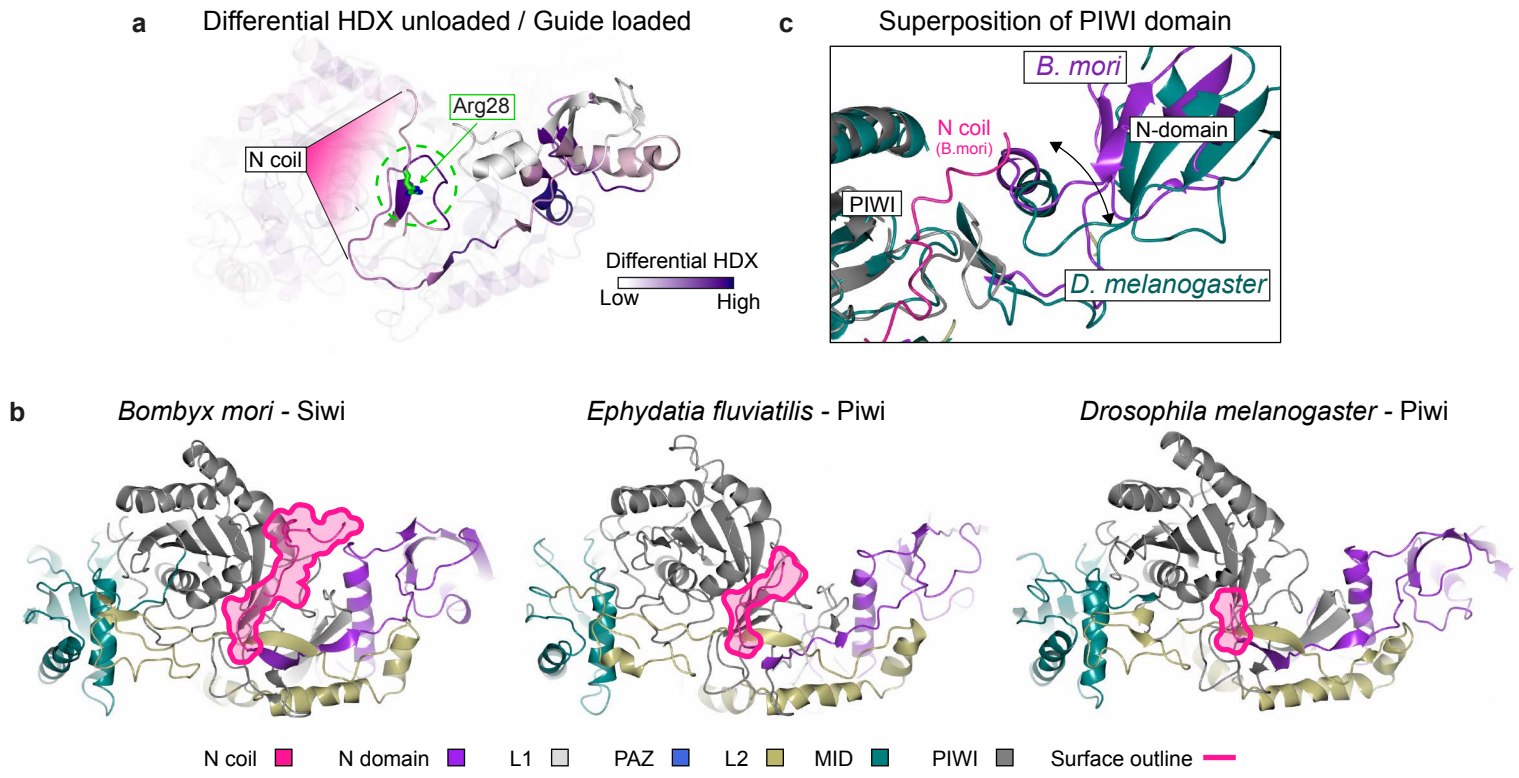

Fig 8. | Structural properties, including flexibility, of the N-coil are recurrent in Ago and Piwi-clade proteins. a, Projection onto the hAgo2 model of the fractional differential hydrogen-deuterium exchange (HDX) data reported by Bibel et al. between unloaded and guide loaded hAgo2[49]. Increasing differences in exchange rate are indicated with progressively darker purple shading. All regions with differential rates of exchange between unloaded and guide-loaded hAgo2 show higher exchange rate in the unloaded state, most notably areas buried by the N-coil and engaging in interactions with N-coil residue Arg28 in the guide-loaded hAgo2. **b**, Structural overview of Siwi and Piwi outlining in pink their N-coils. The *Ephydatia fluviatilis* and *Drosophila melanogaster* Piwi proteins harbour N-coil truncations, probably generated by proteolysis during sample preparation for structural studies. **c**, Secondary structure matching of the *B. mori* and *D. melanogaster* Piwi domains reveals a more relaxed state of the *D. melanogaster* Piwi molecule (green) in which the structurally fixed N-coil seen in *B. mori* Siwi is absent.